

# Understanding and Controlling the Photoluminescence Line Shapes of 2D Perovskites with Chiral Methylbenzylammonium-Based Cations

Lucas Scalon, Arianne New, Ziyuan Ge, Navendu Mondal, Raquel Dantas Campos, Claudio Quarti, David Beljonne, Ana Flávia Nogueira, Artem A. Bakulin,\* and Yana Vaynzof\*

Cite This: <https://doi.org/10.1021/acs.chemmater.3c03234>

Read Online

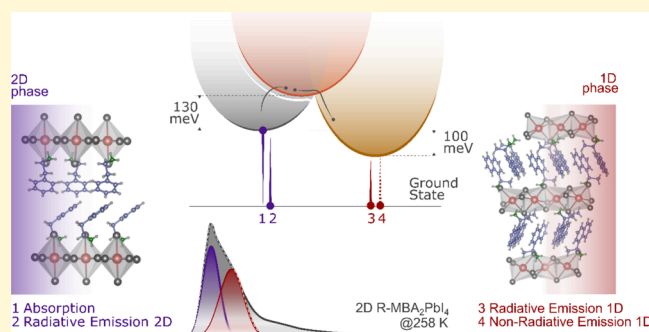
ACCESS |

Metrics & More

Article Recommendations

Supporting Information

**ABSTRACT:** Chiral two-dimensional (2D) perovskites are a promising material class for the next generation of spintronic and chiroptical devices. Despite their promise, many aspects related to film formation and crystallization remain elusive. When chiral ammonium-based organic cations such as methylbenzylammonium (MBA) are employed in the preparation of chiral 2D perovskites, their interaction with the halide species in the inorganic perovskite network often introduces substantial steric hindrance, leading to the formation of one-dimensional (1D) phase impurities within the 2D matrix. Here, we demonstrate that this 1D phase manifests itself in the photoluminescence (PL) spectra of the 2D perovskite film as an additional weakly emissive, thermally activated state with a self-trapped excitonic character, leading to an asymmetric PL response. We demonstrate that the strategic introduction of a methoxy (OMe) group on the *para* position of the MBA cations can mitigate the formation of the 1D phase. As a result, the emission band becomes narrower and more symmetric and the 2D perovskite film has a higher PL quantum yield at room temperature. Our findings elucidate the origins of asymmetry and broadband emission of MBA-based chiral 2D perovskites and highlight the indispensable role of molecular design in chiral organic cations in controlling phase purity and attaining the desired optical properties.



## 1. INTRODUCTION

Metal halide perovskites have attracted significant attention from both the academic and industrial communities due to their high potential for applications in optoelectronic devices, such as solar cells<sup>1–3</sup> and light-emitting diodes (LEDs).<sup>4–6</sup> Perovskites have the general chemical formula  $ABX_3$ : the A-site cation is a monovalent organic or inorganic cation (e.g., formamidinium, methylammonium, cesium, etc.), the B-site cation is a divalent metal (e.g.,  $Pb^{2+}$  or  $Sn^{2+}$ ), and the X-site anion is a halide anion. A great advantage of these materials is the possibility to tune their optoelectronic properties by adjusting the A, B, and X species. For instance, by using a bulky A-site ammonium-based organic cation and controlling the stoichiometry, it is possible to transition from a three-dimensional (3D) cubic structure to a layered two-dimensional (2D) and even polymer-like one-dimensional (1D) structures.<sup>7</sup> The latter have the chemical formulas  $A'_2A_{n-1}B_nX_{3n-1}$  and  $A'BX_3$ , respectively, where  $A'$  is the bulky A-site cation. By decreasing the dimensionality, the exciton quantum confinement increases, leading to enhanced many-body effects and the formation of stable electron–hole pairs (excitons). This, in turn, changes the electronic structure as well as excited-state dynamics, allowing the tuning of photophysical properties such

as the charge carrier transport and photoluminescence quantum yield, depending on the dimensionality and the molecular structure of the chosen  $A'$  cation.<sup>8</sup>

Recent years have witnessed a growing interest in the introduction of chiral organic cations for perovskite nanomaterials with the intention to trigger chiroptical properties, as these are often desired in spintronics and polarization optics applications.<sup>9–12</sup> The chiral organic cation transfers chirality to the inorganic sheets of the perovskite through an asymmetric hydrogen-bonding interaction between the hydrogen in the ammonium group of the organic cation and the halide anion in the inorganic network of the perovskite.<sup>13,14</sup> This breaks the inversion symmetry operation of the crystal and induces changes in the electronic structure, driving, in particular, Rashba splitting of the spin states in the reciprocal space,

Received: December 19, 2023

Revised: March 12, 2024

Accepted: March 12, 2024

which triggers chiroptical properties in the material. For instance, the material will experience different absorption and emission of left- and right-handed circular polarized light and chiral-induced spin selectivity. Recently, we also demonstrated that enantio-enriched cations (i.e., *R*- and *S*-enantiomers) can impact a broad range of properties of the material in comparison to the corresponding achiral racemic (*rac*-) mixture. These properties include phase purity, residual lattice strain, and electronic disorder.<sup>15</sup>

While most of the reports exploring chiral perovskites are focused on device applications<sup>17,16–18</sup> or attempt to understand chirality transfer mechanisms,<sup>19–21</sup> fewer are devoted to understanding their photophysics and structure–function relationships. In the context of the latter, the control over phase purity in regular nonchiral 2D perovskites has been extensively documented, with a focus either on the solvent used for deposition<sup>22</sup> or on the organic cation.<sup>23–25</sup> However, introducing a chiral cation alters the formation dynamics of the low-dimensional perovskite and the obtained products. While the chiral cation imparts chirality on to the inorganic network of the perovskite, it also introduces a higher steric hindrance for the ammonium group to interact with the inorganic network. This is because the ammonium group in the chiral cation typically is at a secondary carbon, as opposed to the conventionally used organic cations like butylammonium and phenylethylammonium, where the ammonium group is at a primary carbon. The resulting steric hindrance impedes the assembly of the 2D structure, facilitating the formation of a 1D phase.<sup>26</sup> Reports on the thin-film characterization of chiral 2D perovskites have consistently shown the coexistence of a 1D phase within the 2D matrix.<sup>27–31</sup> However, a model describing the impact of the 1D phase on material photochemistry has not been proposed. It should be highlighted that although in some works the 1D phase is not observed in diffraction experiments, it does not signify that this phase is absent and does not contribute to the optoelectronic properties. Importantly, our recent findings emphasize that the solvent and temperature used for layer fabrication impact the material properties, which may be mediated by the appearance of the 1D phase.<sup>15</sup>

A characteristic but controversial feature of chiral perovskites is a broad photoluminescence band extending toward lower energies.<sup>32,33</sup> While similar tails are sometimes observed in achiral 2D perovskites and are commonly attributed to lattice deformation,<sup>34</sup> defect-associated and STE emission,<sup>35</sup> and electron–lattice coupling,<sup>36</sup> the origin of the asymmetry in the PL of chiral 2D perovskites remained unidentified. In the following, we show that these effects alone cannot fully account for the observed broadband emission in chiral 2D perovskites based on methylbenzylammonium cations. We examine in detail the photophysical properties of chiral 2D perovskites based on two different chiral cation derivatives and investigate the source of the asymmetry of their emission. Specifically, we focus either on *R*-, *S*-, and *rac*- $\alpha$ -methylbenzylammonium (MBA) or on *R*-, *S*-, and *rac*-*para*-methoxy- $\alpha$ -methylbenzylammonium (*p*OMeMBA) cations (Figures 1a and 1b). They differ only in the presence of an electron-donating methoxy (–OMe) substituent in the *para* position. Some investigations suggested that its presence could decrease the  $\pi$ – $\pi$  stacking interactions between molecules because –OMe drives an increase in the electrostatic repulsion between electron clouds of higher electron densities in the phenyl rings.<sup>37–39</sup> By utilizing a variety of spectroscopic techniques complemented by theoretical calculations, we reveal a direct

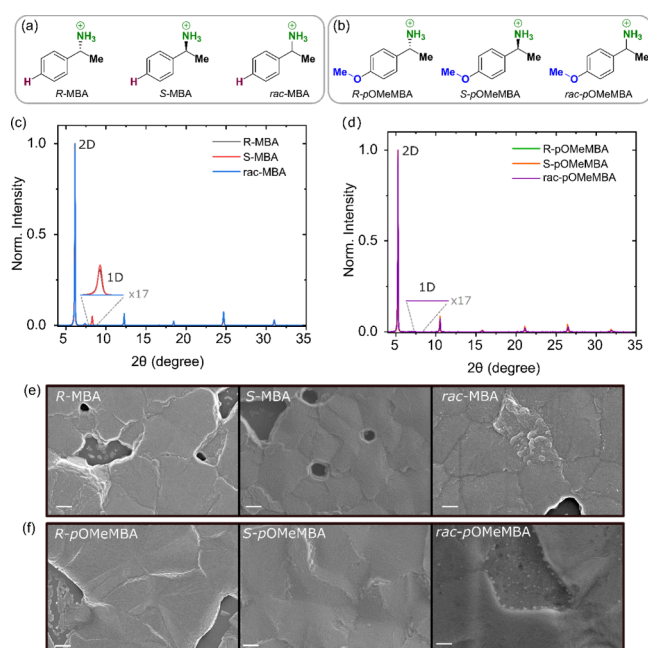


**Figure 1.** Chemical structure of (a) *R*-, *S*-, and *rac*- $\alpha$ -methylbenzylammonium (MBA) and (b) *R*-, *S*-, and *rac*-*p*-methoxy- $\alpha$ -methylbenzylammonium (*p*OMeMBA). Thin-film XRD of (c) *R*-, *S*-, and *rac*-(MBA)<sub>2</sub>PbI<sub>4</sub> and (d) *R*-, *S*-, and *rac*-(*p*OMeMBA)<sub>2</sub>PbI<sub>4</sub>. Scanning electron microscopy (SEM) images of (e) *R*-, *S*-, and *rac*-(MBA)<sub>2</sub>PbI<sub>4</sub> and (f) *R*-, *S*-, and *rac*-(*p*OMeMBA)<sub>2</sub>PbI<sub>4</sub>. The scale bar is 400 nm.

correlation between both PL characteristics and the presence of the 1D phase within the 2D matrix. Strikingly, when we employ the *R*-, *S*-, or *rac*-*p*OMeMBA cation to mitigate the formation of the 1D phase, we observe a notable decrease in both the full width at half maximum (FWHM) and the asymmetry of the PL spectrum. This positive outcome is accompanied by a significant increase in the PL quantum yield as compared to that of 2D perovskites based on the MBA cation.

## 2. EXPERIMENTAL METHODS

Lead(II) iodide (99.999%) and hydroiodic acid (57 wt %) were purchased from TCI Chemicals. *R*-, *S*-, and *rac*-methylbenzylamine and *R*-, *S*-, and *rac*-*p*-methoxymethylbenzylamine and the solvents were purchased from Sigma-Aldrich. All materials were used as received without purification.

**Synthesis of the Iodide-Based Salts.** To a 25 mL round-bottom flask equipped with a magnetic stir bar, 4 mmol of the corresponding amine (either *R*-, *S*-, and *rac*-methylbenzylamine or *R*-, *S*-, and *rac*-*p*-methoxymethylbenzylamine) was poured into 5 mL of isopropanol and cooled to 0 °C in an ice bath. The solution was stirred for 15 min, and then 4.4 mmol of the HI solution (57 wt % in water) was added dropwise. The reaction was kept in the ice bath for 1 h and then allowed to reach room temperature inside the ice bath. After reaching room temperature, the solvent was evaporated, and a brownish solid was obtained. This solid was washed several times using diethyl ether, which allows for the removal of HI and its byproducts. At the end of this step, a white (or yellowish) powder is obtained. To ensure the removal of all HI residues, we performed several recrystallization steps, consisting of dissolving the obtained powder in a minimal amount of hot isopropanol and slowly cooling it down to room temperature. In the presence of HI residues, the solvent after recrystallization has a slightly yellow color. This procedure is repeated at least three times. Finally, the powder was

recovered, washed three times with 50 mL of diethyl ether, and dried in a vacuum oven at 50 °C for 8 h.

**Preparation of *R*-, *S*-, and *rac*-(MBA)<sub>2</sub>PbI<sub>4</sub> (MBA: Methylbenzylammonium) and *R*-, *S*-, and *rac*-(*p*OMeMBA)<sub>2</sub>PbI<sub>4</sub>.** To a vial were added 2 mmol of the corresponding iodide-based ammonium salt and 1 mmol of PbI<sub>2</sub> in 1 mL of anhydrous DMF. This solution was stirred with a vortex for 5 min and then allowed to sit for 30 min. Next, 50 μL of the chiral 2D perovskite precursor solution was spread onto a 1.5 × 1.5 cm<sup>2</sup> glass substrate. Before this step, the substrate was cleaned with Hellmanex, acetone, and isopropanol and treated in an ozone chamber for 10 min. For the deposition process, a two-step spin-coating program was employed: 1000 rpm, 10 s, 500 rpm/s and 4000 rpm, 30 s, 1000 rpm/s. After the end of the spin-coating step, the substrate was immediately transferred to a hot plate set at 100 °C and annealed for 10 min.

**Preparation of *R*-, *S*-, and *rac*-(MBA)PbI<sub>3</sub> Thin Films.** To a 5 mL vial, 56 mg (0.22 mmol, 0.75 equiv) of the *R*-, *S*-, or *rac*-methylbenzylammonium iodide, 138.3 mg (0.30 mmol, 1 equiv) of PbI<sub>2</sub>, and 1 mL of DMF were added. This creates a 0.3 M precursor solution of the 1D perovskite. The solution was stirred at room temperature for ~2 h and deposited by spin-coating onto a glass substrate at 1000 rpm, 10 s, with 500 rpm s<sup>-1</sup> of acceleration followed by 4000 rpm, 30 s, with 1000 rpm s<sup>-1</sup> of acceleration. Right after the end of the spin-coating, the films were placed in a hot plate for thermal annealing at 100 °C for 10 min.

**Preparation of *R*-, *S*-, and *rac*-(*p*OMeMBA)PbI<sub>3</sub> Thin Films.** To a 5 mL vial, 41.5 mg (0.15 mmol, 0.5 equiv) of the *R*-, *S*-, or *rac*-methylbenzylammonium iodide, 138.3 mg (0.30 mmol, 1 equiv) of PbI<sub>2</sub>, and 1 mL of DMF were added. This creates a 0.3 M precursor solution of the 1D perovskite. The solution was stirred at room temperature for ~2 h and deposited by spin-coating onto a glass substrate at 1000 rpm, 10 s, with 500 rpm s<sup>-1</sup> of acceleration followed by 4000 rpm, 30 s, with 1000 rpm s<sup>-1</sup> of acceleration. Right after the end of the spin-coating, the films were placed in a hot plate for thermal annealing at 100 °C for 10 min.

**X-ray Diffraction (XRD).** XRD patterns were measured in ambient air using a Bruker Advance D8 diffractometer equipped with a 1.6 kW Cu anode ( $\lambda = 1.54060 \text{ \AA}$ ) and a LYNXEYE\_XE\_T 1D detector. The scans were measured in a parallel beam geometry with a height-limiting slit of 0.2 mm. For grazing-incidence XRD the incidence angle ( $\Omega$ ) was fixed at 0.2°, 0.5°, 1°, and 1.5°.

**UV–Vis Absorption, Photoluminescence Emission, and Photoluminescence Excitation Measurements.** Temperature-dependent PL emission spectra were measured with a continuous-wave 405 nm laser at 100 μW, a 450 nm long pass filter, a neutral density filter, and a Linkam stage flushed with nitrogen gas. The temperature was lowered from room temperature (298.15 K) to liquid nitrogen cryogenic temperatures (78.15 K), 10 K at a time.

**Circular Dichroism (CD).** CD spectra were recorded at 20 °C in a JASCO J-720 spectropolarimeter using a Xe lamp as the light source.

**Electronic Structure Calculations.** The band structure in Figure 7 is obtained by using periodic DFT calculations, within the plane-wave/pseudopotential formalism, as implemented in the Quantum-Espresso suite. A cutoff of 50 Ry was used for the plane-wave expansion, along with fully relativistic norm-conserving pseudopotentials, as available from the pseudodojo database. Spin–orbit coupling is clearly included in the calculation, as an unavoidable ingredient to retrieve the spin splitting associated with the Rashba effect. All calculations are performed using the PBE functional to describe the exchange–correlation interaction. This is known to underestimate the single-particle band gap of 2D lead halide perovskites but provides band dispersions and effective masses in reasonable agreement with the experiment. Periodic models for the racemic and *R*-enantiomeric (MBA)<sub>2</sub>PbI<sub>4</sub> 2D halide perovskites are taken from XRD structures from refs 27 and 70, respectively. We used 4 × 4 × 4 and 4 × 4 × 2 automatic sampling of the Brillouin zone for the racemic and *R*-enantiomeric compound, respectively, the different sampling of the reciprocal vectors reflecting the anisotropy in the direct lattices.

### 3. RESULTS AND DISCUSSION

**Structural Characterization.** Thin films of *R*-, *S*-, and *rac*-(MBA)<sub>2</sub>PbI<sub>4</sub> (MBA:  $\alpha$ -methylbenzylammonium) and *R*-, *S*-, and *rac*-(*p*OMeMBA)<sub>2</sub>PbI<sub>4</sub> (*p*OMeMBA: *p*-methoxy- $\alpha$ -methylbenzylammonium) were prepared by mixing 0.6 M of the correspondent iodide-based salt of the organic cation with 0.3 M of PbI<sub>2</sub> in dimethylformamide (DMF). The chemical structures of the organic cations are shown in Figure 1a,b. The two classes of low-dimensional chiral perovskites differ in the presence of the –OMe group in the *para* position of the phenyl ring. The resonance hybrids of *p*OMeMBA (Figure S1) explicitly show that the –OMe group introduces a negative charge in the phenyl ring and a positive charge in the oxygen atom, confirming that the methoxy group has an electron-donating character.

X-ray diffraction (XRD) measurements were used to assess the crystallinity of the chiral perovskite films (Figure 1c,d). For both MBA and *p*OMeMBA, the 2D perovskite grows in the [001] plane stacking direction. However, the interlayer distance between the lead octahedra sheets (calculated for the (001) diffraction plane) increases from ~14 to ~17 Å from MBA to *p*OMeMBA due to the larger volume of the latter. These values are close to but not exactly as those predicted by the size of each molecule. The sizes of MBA and *p*OMeMBA can be estimated by measuring the distance between the two most distant atoms, which yields 7.2 and 9.1 Å, respectively (Figure S2). Therefore, the predicted value for the distance between the lead octahedra sheets should be approximately equivalent to double the cation size—as we are using monovalent cations that generate Ruddlesden–Popper-type low-dimensional perovskites (chemical formulas A<sub>2</sub>A<sub>*n*-1</sub>Pb<sub>*n*</sub>I<sub>3*n*+1</sub>). Based on this analysis, the experimental interlayer distance for the MBA-based perovskites is 2.8% lower than expected (14.4 Å, corresponding to two times the size of a single MBA cation), whereas for the *p*OMeMBA-based perovskites, it is 6.4% lower (18.2 Å, corresponding to two times the size of a single *p*OMeMBA cation). Recently, Vázquez-Cárdenas et al.<sup>40</sup> observed a similar trend for phenylethylammonium and its *p*-methoxy-substituted cations, with the latter resulting in a higher interlayer distance deviation than the former. In light of this, we speculate that the discrepancy in terms of interlayer distance can be related to variations in crystal size and a more favorable crystal packing of the 2D perovskite when *p*OMeMBA is used.<sup>40</sup> It is also important to highlight that the halogen-bonding interaction between the methoxy group and the iodide may influence the shrinkage of the lead octahedral interlayer distance. This interaction can benefit the electronic coupling between the inorganic sheets, thereby increasing charge carrier delocalization.<sup>41</sup>

We used the Williamson–Hall equation (eq 1) to calculate the residual lattice strain in these two classes of perovskites.<sup>42–44</sup> Here,  $\beta$  is the FWHM of the XRD peaks,  $\theta$  is the diffraction angle in rad,  $\epsilon$  is the residual strain of the lattice, and  $K$ ,  $\lambda$ , and  $D$  are the Scherrer constant, the X-ray wavelength, and the crystallite size, respectively. Following the trend observed in our previous report,<sup>15</sup> enantiomerically pure *R*- and *S*-perovskites have lower strain compared to the racemic mixtures (Figure S3). 2D perovskites prepared from MBA-based cations also exhibit about 30% lower residual strain than their *p*OMeMBA counterparts. The reasons for these differences remain to be investigated, but we speculate

that asymmetric hydrogen bonding, which is expected to impact octahedra tilting, may be the origin of such differences.

$$\beta \cos(\theta) = \epsilon[4 \sin(\theta)] + \frac{K\lambda}{D} \quad (1)$$

In addition to the reflections corresponding to the (00*l*) planes, *R*- and *S*-(MBA)<sub>2</sub>PbI<sub>4</sub> present an additional peak at 8.3° (see the inset in Figure 1c), which can be assigned to 1D polymeric face-sharing chains of (MBA)PbI<sub>3</sub>.<sup>27</sup> In contrast, the XRD spectra of the chiral *p*OMeMBA-based 2D perovskites do not show any evidence of the 1D phase (Figure 1d), which points out that the introduction of an electron-donating substitute may prevent the formation of the 1D phase in the 2D matrix.

There are several plausible explanations for the lower formation of the 1D phase in *p*OMeMBA-based 2D perovskites. Previous investigations exploring the control of phase dispersity in quasi-2D perovskites show that the introduction of the *p*OMe substituent can enhance the intermolecular interactions between the cation and the lead species in the perovskite precursor solution, thereby providing better control of phase dispersity and purity.<sup>40,45</sup> In addition, the methoxy group activates the *meta* and *para* positions (Figure S1), meaning that the resonance hybrids have a negative charge at these positions of the phenyl ring. The presence of the negative charge at the *para* position ( $\beta$ -carbon to the ammonium group) may decrease the positive charge on the nitrogen atom compared to the MBA cation. This increases the *pK<sub>a</sub>* of *p*OMeMBA as compared to that of MBA, making the former a weaker acid. We speculate that this feature may also contribute to restricting the formation of the 1D phase. Furthermore, the presence of the -OMe group increases the dipole moment on the molecule. This feature facilitates the end-to-end self-assembly of the molecules through H-bonding,<sup>46</sup> which may facilitate the assembly of 2D structures. Nevertheless, further research is required to elucidate all of the complex intricacies of crystallization and film formation in this case.

Importantly, the absence of 1D reflexes from the XRD spectra does not necessarily indicate that this phase is not present in the films, as it may be below the detection limit of XRD. However, it suggests that the amount of 1D phase within the *p*OMeMBA-based 2D perovskites is reduced compared to that in the MBA-based perovskites. It is important to note that various parameters can influence the formation of 1D phase within the 2D matrix. In our recent work, we demonstrated that the choice of solvent used for the preparation of the 2D perovskite films, such as dimethylformamide (DMF) or acetonitrile (ACN), and the crystallization conditions (whether at room temperature or upon thermal annealing) can have a significant impact on properties such as the conductivity of the samples and their energetic disorder.<sup>15</sup> We found that films deposited from ACN exhibited a higher amount of the 1D phase, confirming that processing conditions can have a high impact on the formation of the 1D phase within the 2D perovskite.

Furthermore, it is crucial to highlight that despite the reduced presence of the 1D phase in the *p*OMe-based 2D perovskites in comparison to the MBA-based ones, it can still be detected by PL measurements, as will be discussed later. Preventing the formation of 1D structures in chiral 2D perovskites is therefore a significant challenge. The difficulty arises from the introduction of chirality in the cations on the  $\alpha$ -carbon adjacent to the -NH<sub>3</sub> group. This leads to greater

steric hindrance in the interaction with the halide on the [MX<sub>6</sub>]<sup>4-</sup> octahedra compared to nonchiral cations, in which the ammonium group is attached to a primary carbon (e.g., hexylammonium and phenylethylammonium).<sup>26</sup> A potential strategy to overcome this challenge could involve the use of molecules where the chiral center is positioned on the  $\beta$ -carbon adjacent to the ammonium group, such as *R*-, *S*-2-(aminomethyl)-4-methylpentanoic and *R*-, *S*-3-amino-2-benzylpropanoic acid. However, further research is necessary to determine whether these cations can effectively impart their chirality to the inorganic network of the perovskite lattice.

We also employed the scanning electron microscopy technique to visualize the microstructural characteristics of the film (Figures 1e and 1f). The images revealed that the films consist of large, smooth grains on the order of 1  $\mu$ m in diameter, yet also exhibit a significant number of pinholes. No clear differences between the microstructures of the MBA-based and the *p*OMeMBA-based perovskites could be observed. The fact that we cannot identify the 1D phase on the surface of the films may be related to the vertical distribution of this phase. As we demonstrated recently, MBA-based chiral 2D perovskite films prepared from dimethylformamide have only a minimal amount of the 1D phase on the surface, becoming more evident in the bulk of the film.<sup>15</sup>

**Steady-State Absorption and Circular Dichroism.** The shape of the UV-vis absorption spectra of both sets of chiral perovskites displays a similar profile dominated by an excitonic absorption at around 500 nm (Figure S4a,b) with only slight differences between the two different types of cations. For example, the FWHM of the excitonic band is slightly narrower for the *p*OMe-based (~27 nm) chiral perovskites as compared to that of the MBA-based ones (~41 nm). Additionally, the optical bandgap (*E<sub>g</sub>*) is slightly higher for *p*OMe-based (2.42 eV) than for the MBA-based samples (2.39 eV). This is related to details in the organization of the inorganic lattice, in particular, to the octahedral tilting as measured by Pb-I-Pb valence angles. Previous investigations indeed demonstrated that deviations from linear Pb-I-Pb bonds translate into less effective atomic hybridization and hence narrower band dispersion and increased charge effective masses.<sup>47-49</sup> The potential influence of interplanar electronic coupling, as induced by the different interlayer distance, is likely disregarded as periodic density functional theory (DFT) calculations indicate an interlayer coupling for shorter distance MBA spacer on the order of meV (vide infra).

The CD spectra were obtained from both film/air and glass/air interfaces. By calculating the semi-sum between the spectra obtained from both sides, it is possible to determine the genuine CD (CD<sub>gen</sub>) (Figure 2) and, consequently, the genuine anisotropic factor (*g*<sub>factor,gen</sub>, Figure S4c,d). These

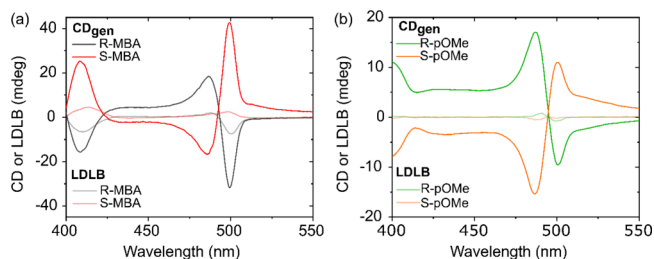


**Figure 2.** Genuine CD and LDLB contributions for (a) *R*-, *S*-MBA<sub>2</sub>PbI<sub>4</sub> and (b) *R*-, *S*-(*p*OMeMBA)<sub>2</sub>PbI<sub>4</sub>.

values are important as they subtract the influence of linear dichroism (LD) and linear birefringence (LB), here called the LDLB contribution, to the CD spectra, which is common for highly oriented systems with a high degree of anisotropy.<sup>50–52</sup>

Figure 2a,b shows the genuine CD spectra and LDLB contributions. We can see that both sets of samples present CD spectra with a derivative line shape changing of sign around the excitonic transition (500 nm). The LDLB contributions are negligible for both sets, being slightly higher for the MBA-based samples, which indicates a higher effect of the macroscopic anisotropies on the CD signal in that case.

Furthermore, we calculate the  $g_{\text{factor,gen}}$  using the equation  $g_{\text{factor,gen}} = \text{CD}_{\text{gen}} / (32980 \times A)$ , in which  $A$  stands for absorbance. The anisotropic factor differs from the CD measurement because it offers information about the ellipticity of the linear polarized light after crossing the chiral sample, whereas CD considers just the differential absorption of left- and right-handed circular polarized light.<sup>53</sup> In addition, the anisotropic factor becomes independent of the sample thickness variation, concentration, and molecular weight,<sup>54</sup> being a better parameter to compare the chirality transfer effects. We found that the maximum  $g_{\text{factor,gen}}$  around the excitonic transition is equal to  $\sim 5.0 \times 10^{-4}$  for *R*- and *S*-MBA and to  $1.2 \times 10^{-4}$  for *R*- and *S*-*p*OMe (see Figure S4c,d for the  $g_{\text{factor,gen}}$  as a function of the wavelength). Therefore, 2D perovskites prepared with MBA-based chiral cations showed a  $g_{\text{factor,gen}}$  of more than 70% higher than those prepared with *p*OMeMBA. The reduction of the anisotropic factor may be related to the increased interlayer distance between the lead octahedra sheets, which influences the chirality transfer because it is mediated by halogen-bonding interactions between H $\cdots$ I,<sup>13</sup> thereby reducing the rotatory strengths and, as a consequence, the magnitude of the anisotropic factor.<sup>54</sup> A recent report suggested that the introduction of heavy atoms at the *para* position of the phenyl ring in MBA can enhance the rotatory strengths even for chiral 2D perovskites with a larger *d*-spacing.<sup>54</sup> However, it should be noted that in that case, differently from what is presented in our work, a series of halogen-substituted *p*-MBA cations were investigated, which could help enhance the rotatory strength in the system due to halogen–halogen interactions with the inorganic network of the perovskite.

**Steady-State PL Spectra.** Figure 3a compares the room temperature PL emission spectra of two perovskite thin films fabricated using a racemic mixture of the cations (the PL emission corresponding to the other samples can be found in Figures S5 and S6). Both samples display similar PL spectra,

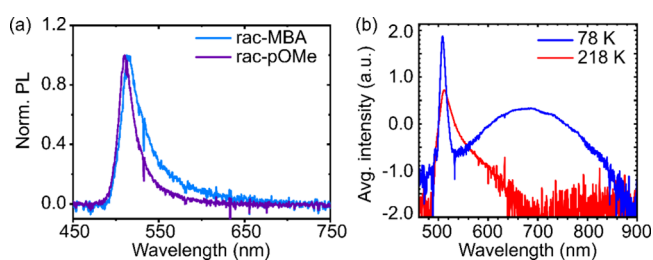


**Figure 3.** (a) Normalized PL spectra at room temperature of *rac*-(MBA)<sub>2</sub>PbI<sub>4</sub> and (*p*OmeMBA)<sub>2</sub>PbI<sub>4</sub>. (b) Log-scaled PL spectra of *rac*-(MBA)<sub>2</sub>PbI<sub>4</sub> smoothed over three points at 218 and 78 K, showing a second peak present at around 535 nm and the emergence of a third peak at around 650 nm.

with a band centered at 518 nm relating to “free” 2D exciton (FE) emission. However, in both samples, a long tail that extends toward lower energies is observed, being less evident for the *p*OmeMBA sample. As a result, the FWHM of the *p*OmeMBA-based perovskites was approximately 27% lower than that of the MBA-based perovskites. Furthermore, the *p*Ome-substituted cations resulted in double the photoluminescence quantum yield (PLQY) compared to the nonsubstituted samples (0.14 vs 0.07%, respectively) (Figure S5). The higher PLQY could be related to the fact that the –Ome group increases the dipole moment of the molecule. This feature is reported to increase carrier dissociation due to narrowing the difference between the dielectric constants of the organic and inorganic layer, which thereby decreases the Coulombic screening of electrons and holes in the inorganic layer.<sup>55,56</sup>

At liquid nitrogen temperatures (78 K) the emission spectrum (Figures 3b and S7) becomes much narrower and more symmetric. The biggest and rather abrupt change is the disappearance of the red-shifted contribution in the 530–550 nm region, accompanied by a strong enhancement of PL intensity, which will be discussed in the following sections. Apart from the main peak, a band at approximately 650 nm can also be identified only at low temperatures (Figures S5 and S7), relating to unreacted PbI<sub>2</sub> and resultant stoichiometric Frenkel defects.<sup>57–59</sup> The PbI<sub>2</sub>-related emission is an amalgamation of multiple peaks and remains at the same position upon cooling, while its intensity increases, implying it is an impurity defect-related emission.

When comparing the MBA- vs *p*OmeMBA-based perovskites, it is noticeable that *p*OmeMBA-based perovskites have narrower emission bands, especially at higher temperatures (Figures S9 and S10), and the PbI<sub>2</sub>-related emission is almost absent (Figure S8). The low emission intensity of the PbI<sub>2</sub>-related band becomes obvious by plotting the log scale of the data obtained in the low-temperature regime (Figure S7). Such behavior suggests the conversion of the precursors into the 2D perovskite is more efficient when the *p*Ome-substituted cation is used, which can be partially attributed to the better solubility of this cation when compared to MBA and due to the fact the methoxy group can enhance the interaction between the organic cation and the lead species in solution,<sup>40,45</sup> as mentioned elsewhere. We speculate that these combined effects, named better solubility and enhanced interaction with the lead species, may slow down the formation of the perovskite film, which benefits the assembly of the 2D layered-stack perovskite.

**Temperature-Dependent PL Spectroscopy.** Temperature-dependent PL measurements were performed from 78 to 298 K to investigate the nature of the broadband emission and to elucidate potential differences between enantiomerically pure and racemic cations. The PL spectra of each sample are in Figures S9 and S10. To simplify, we compare in Figure 4 the PL emission and PL spectral shape only for the *R*-(MBA)<sub>2</sub>PbI<sub>4</sub> and *R*-(*p*OmeMBA)<sub>2</sub>PbI<sub>4</sub> perovskite films. These spectra show that the PL intensity increases, and the main peak narrows as the temperature decreases. We speculate that both trends are likely related to the same process that reduces the FE radiative relaxation pathway and meanwhile promotes radiative and nonradiative decay from different electronic states at room temperature. Additional contributions to PL spectral shape and intensity may arise from the temperature-induced modulation of electron–phonon coupling effects.<sup>59–61</sup>

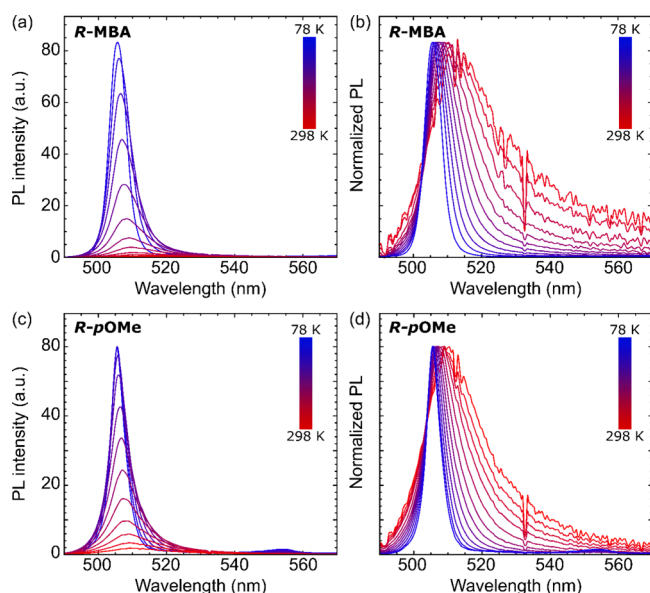


**Figure 4.** Temperature-dependent PL emission of (a, b)  $R$ -(MBA) $_2$ PbI $_4$  and (c, d)  $R$ -( $p$ OMeMBA) $_2$ PbI $_4$  every 20 K (left panels) and normalized (right panels), showing the increase in intensity, decrease in FWHM, and blue-shift as temperature decreases. The data for the other samples are shown in Figures S8–S10.

The dominant effect on the PL emission spectral width arises from the previously identified red-shifted emission feature, which is particularly evident at higher temperatures. As mentioned above, at room temperature, in addition to the FE emission, a strong contribution at approximately 535 nm is observed. These two contributions are clearly seen by fitting the PL spectra with Voigt functions (Figure S11). As evinced in Figure 4, as the temperature decreases, the FE band blue-shifts, peaking at 505 nm at 78 K. The shoulder at 535 nm follows the same trend, but its total and relative intensity decrease with temperature, until it becomes nonobservable below 200 K. Such a trend is present for both cations; it is thus only weakly dependent on the organic cation spatial configuration. By comparing the integrated intensity of the shoulder, we notice that its contribution to the total emission is smaller for the  $p$ OMeMBA-based perovskites than for the MBA-based perovskites. This finding suggests that the emission at 535 nm is primarily responsible for the broadening of the PL emission band and can be controlled by the addition of the methoxy group to the MBA cation. Below 200 K, the emission can be described by a bimodal shape with small interpeak separation, typical for the presence of longitudinal optical (LO) phonons, which often have energies on the scale of 10 meV.<sup>62,63</sup> Importantly, the 535 nm shoulder is a large energy difference away from the main peak at high temperatures ( $\sim 20$  nm) and thus cannot be explained by phonons, suggesting the formation of a new electronic state.

As the low-energy shoulder responsible for the high bandwidth and asymmetry of PL emission appears to be related to a temperature-activated process, we performed a quantitative analysis of the integrated area under the FE emission and the shape of PL emission based on the Arrhenius and independent Boson models. Figure 5a shows the dependence of the integrated FE emission as a function of the inverse temperature. The FE emission drops exponentially when the temperature increases above 200 K ( $1/T = 0.005$ ), which is a clear indication that the nonradiative relaxation

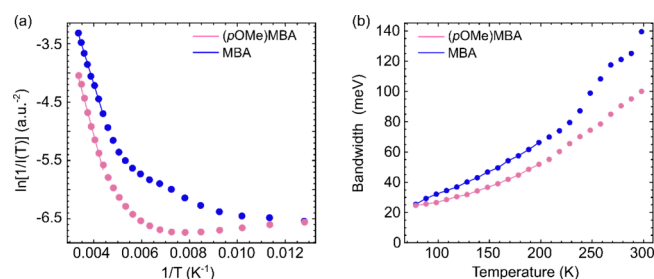


**Figure 5.** (a) Linear fits of the integrated area under the temperature-dependent PL curve within the integral boundaries of  $\pm 20$  nm from the peak maxima, for  $rac$ -(MBA) $_2$ PbI $_4$  ( $E_a = 115$  meV) and  $rac$ -( $p$ OMeMBA) $_2$ PbI $_4$  ( $E_a = 133$  meV). (b) Analogous temperature-dependent FWHM of the PL spectra.

pathway is becoming activated. Therefore, the Arrhenius fitting of the high-temperature part of the graph provides the estimate of the barrier between the FE and the nonradiatively relaxing state. The values found are similar for both perovskite materials at 115 meV for  $rac$ -(MBA) $_2$ PbI $_4$  and 133 meV for  $rac$ -( $p$ OMeMBA) $_2$ PbI $_4$ .

Besides a decrease in intensity as the sample is heated from 78 K, the bandwidth increases as well (Figure 5b), and so does the peak asymmetry. The asymmetry of the PL spectra is most likely associated with a combination of effects including the thermal activation of phonon modes (dominant at low temperatures) as well as the thermally activated population of an additional electronic state (dominant at high temperatures). The overall PL reduction indicates that this new state undergoes mostly nonradiative recombination. However, the relative enhancement of emission in the region of 535 nm at high temperatures ( $> 200$  K) suggests the possible presence of a relatively inefficient but measurable radiative pathway with red-shifted emission, which is likely mediated by the temperature-activated energy transfer to an electronic state different from the 2D free excitons. In the temperature region below 200 K, the PL emission intensity does not change substantially and probably can be described by a single electronic state/relaxation pathway. Fitting the low-temperature part of Figure 5b with the independent Boson model can provide an estimate of electron phonon-coupling strength and the energy of the most coupled phonon. For  $R$ -(MBA) $_2$ PbI $_4$  and  $R$ -( $p$ OMeMBA) $_2$ PbI $_4$  we obtained reasonable LO phonon energy values of 30 and 40 meV, respectively.

**Two-State Model and Transient Absorption Data.** As discussed above, the temperature-dependent PL data suggest the existence of another electronic state, in addition to the FE, in the 2D perovskite. The population of this state is temperature-activated and positioned about 130 meV above the FE (see the Arrhenius fitting in the previous section). At the same time, the PL emission from this state observed in the  $\sim 535$  nm region is very weak (i.e., nonradiative relaxation dominates) and is approximately 100 meV red-shifted from the main FE emission band (see Figure S11). This is strong evidence that the additional state is mostly “dark” in terms of emission and has a strong self-trapped exciton (STE) character.

The photophysical model that we propose to explain the temperature-dependent PL trends is presented in Figure 6a. It is based on the model for self-trapped excitons and can be seen as an extension of the models previously proposed in the literature.<sup>59,64,65</sup> The model includes a bright (i.e., strong

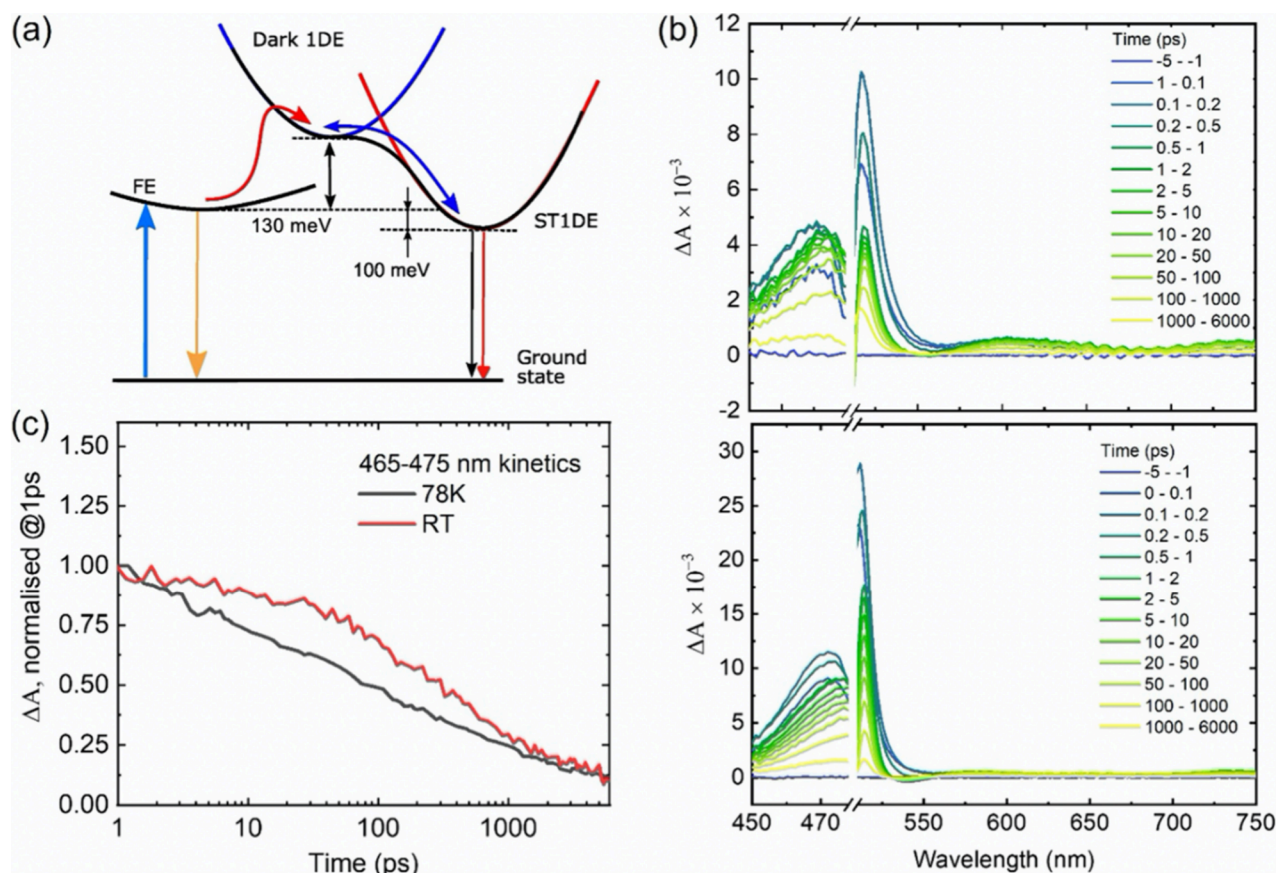


**Figure 6.** (a) Suggested two-state model explaining the temperature-related trends in PL intensity, spectral shape, and dynamics. The blue and orange arrows indicate the transitions between the FE and the ground state. The black and red arrows from the ST to the ground state indicate the radiative and nonradiative relaxation that can occur, respectively. (b) TA spectra of  $R\text{-(MBA)}_2\text{PbI}_4$  at RT (top) and 78 K (bottom). (c) Dynamics of the FE state at RT and 78 K based on the TA data.

radiative and weak nonradiative relaxation) FE state as well as a higher-energy “dark” (i.e., weak radiative and strong nonradiative relaxation) exciton state with the pronounced STE character. The dark state becomes populated by the FE state in a process that can occur with a substantial energy barrier ( $\sim 130$  meV).<sup>66</sup> The lifetime of the STE state is probably substantially longer than the FE lifetime. The weak emission and strong nonradiative relaxation from the dark state dominate the PL response at room temperature when the transfer from the FE state to the dark state (and back) is allowed and the two states stay in equilibrium. As a consequence, the weak emission from the dark (or weakly active) state is responsible for the asymmetry of the PL spectra at higher temperatures. We note that STE in deformable lattices results in a highly distorted excited state with respect to the ground state.<sup>67</sup> An increase in the metal–halide overlap leads to a stronger increase in the valence band energy relative to the conduction band and, therefore, to a decrease in the  $E_g$  energy.<sup>59</sup>

To verify the proposed model, we performed the transient absorption (TA) experiments presented in Figure 6b. Both 78 and 298 K spectra are dominated by photoinduced absorption (PIA) across the complete probe region. Most PIA features evolve in the same time scale, which we associate with the FE dynamics. We note the presence of short-time dynamics near the band edge, which is associated with exciton cooling. However, this phenomenon goes beyond the scope of this study. We therefore focus on the PIA dynamics at 470 nm and

interpret the signal as being proportional to the population of the FE state. Figure 6c compares the dynamics of the FE state population as a function of time in 2D perovskites fabricated by using the  $R\text{-MBA}$  cation at low and room temperatures. Rather surprisingly, the decay of the population is slower at room temperature despite the significantly lowered PL yield, and the substantially accelerated nonradiative processes. This confirms the model presented in Figure 6a, where the population of the relatively long-lived dark state can serve as a reservoir for the excited states. The thermally activated two-way transfer processes between the FE and the dark state allow for the “storage” of the excited states and their later release through FE emission. At 78 K, the transfer to the dark state is largely forbidden because the thermal energy at this temperature is not enough to overcome the activation energy to the dark state, making the fast and efficient radiative relaxation of FE the only channel to the ground state.

**Origin of the Red-Shifted Emission.** Based on the model presented in previous sections, the red-shifted asymmetric PL at room temperature originates from a weak dark state emission. However, the nature of this dark state is yet unclear. In principle, the broadband emission of the  $[00L]$  oriented 2D perovskites can be related to several factors, such as increased electron–phonon coupling,<sup>66</sup> the recombination of FE and self-trapped excitons,<sup>68</sup> the contribution of halide-vacancy-related emission,<sup>69</sup> increased effect of reabsorption at room temperature, or even the presence of bulk vs surface states. However, the hypothesis that electron–phonon coupling has a

dominant effect is not consistent with our transient absorption data and the overall model presented in Figure 6a. Halide vacancies and self-trapped excitons are also expected to be lower in energy than the FE state, and their emission should not be temperature-activated, unlike what we observe. Furthermore, the effects of increased reabsorption should also not be dominant in the thin samples studied here.

Other possible scenarios for the red-shifted emission can be related to the band splitting in chiral perovskites or the presence of a 1D phase in the 2D matrix serving as an energy-activated energy trap for excitonic states. To evaluate the possible effects of band splitting, we performed density functional theory (DFT) calculations on ideal periodic 2D halide perovskite models (without defects). For this purpose, we considered the  $(\text{MBA})_2\text{PbI}_4$  2D halide perovskite, which represents the ideal model system for the chiral 2D perovskite, as both the phases incorporating the pure *R*-/*S*-MBA enantiomer and the racemic form have been fully resolved via XRD measurements.<sup>27,70</sup> The band structure of the racemic and *R*-enantiomer of  $(\text{MBA})_2\text{PbI}_4$  in Figure 7 agrees well with

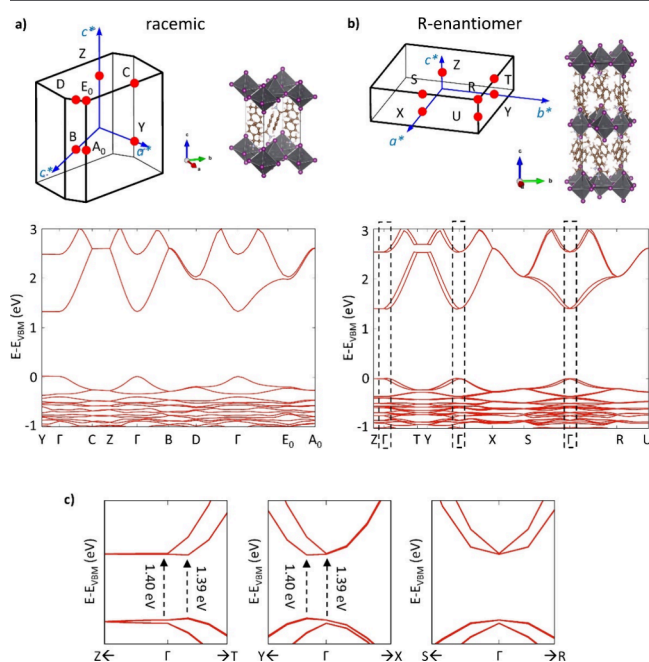


**Figure 7.** (a) Unit cell and first Brillouin zone and corresponding band structure for the racemic  $(\text{MBA})_2\text{PbI}_4$  2D halide perovskite. (b) Same for the pure *R*-enantiomer form. (c) Zoom of the band dispersion of the *R*- $(\text{MBA})_2\text{PbI}_4$  structure close to the center of the Brillouin zone.

previous reports,<sup>14</sup> with a clear signature of quantum confinement as related to the flat dispersion in the reciprocal direction associated with the plane stacking direction ( $Y \rightarrow G$  and  $Z \rightarrow G$  for the racemic and pure *R*-enantiomer compound, respectively). The racemic compound shows a direct band gap at the  $G$  point, while the *R*-enantiomer shows Rashba spin splitting of the frontier levels. The presence of spin splitting is a straight consequence of the incorporation of the pure enantiomer of MBA, as this leads to loss of inversion symmetry (in the model proposed by Billings, inversion symmetry relates the *R*-/*S*-forms of the MBA spacer in the crystal structure of the racemic compound). Therefore, the Rashba splitting cannot be invoked to explain the asymmetry in the PL spectra,

as it should manifest only for the compound containing the pure enantiomer form, and here the asymmetry was observed independently on the spatial configuration of the organic cation. Moreover, the relaxation of free charges from the high symmetry point to the valence and conduction band edges is, in the first approximation, a barrierless process, and the energy difference between the lowest energy direct transition and the transition at  $G$  (10 meV) is inconsistent with the energy difference extracted from the PL data (see Figure 6a).

We now move to an exciton picture, which is more suitable to discuss the optical properties of 2D halide perovskites. Another intrinsic mechanism that may explain the 100 meV red-shifted contribution in the PL is related to the relaxation toward a weakly bright state below the main optically allowed resonance. The presence of a dark (or weakly active) component in the fine structure of the lowest energy exciton is indeed anticipated by symmetry analysis,<sup>71</sup> with both magneto-absorption measurements<sup>72</sup> and ab initio BSE calculations<sup>73</sup> confirming its presence below the most intense FE resonance. On the other hand, the dark–bright energy splitting reported from the literature (9 meV<sup>72</sup>–18 meV<sup>73</sup>) is not consistent with the energy scale of 100 meV. Furthermore, the bright-to-dark relaxation process should also be barrierless, unless invoked by two-phonon relaxation mechanisms, as in the case of 3D halide perovskites.<sup>74</sup>

Ruling out the above explanations, we suggest that the dark state controlling the emissive properties of the studied material at room temperature can be the excitonic state (1DE) of the low concentration of the 1D perovskite phase present in the samples. The energy of 1DE is noticeably higher than the FE in the 2D phase; however, the absorption tail on 1DE spreads to the green spectral region, making the transfer from FE to 1DE possible with thermal energy. The 1DE is known for relatively low PL, a large Stoke's shift, strong STE character, and long-lived emission, which agree well with the two-state model presented above. Moreover, the 1D phase is thermodynamically favorable,<sup>75–77</sup> thus often unintentionally forming during the 2D perovskite fabrication.

To verify the hypothesis that the 1D phase serves as a temperature-activated dark reservoir of excitonic states at high temperatures, we have performed PL spectroscopy of on-purpose prepared 1D perovskites (see the Supporting Information for details). Figure 8a shows that 1D *R*-

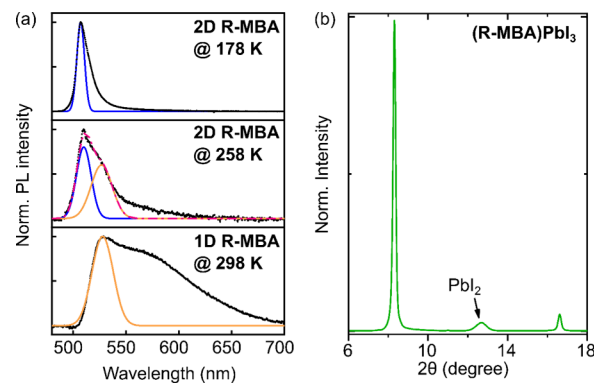


**Figure 8.** (a) PL spectra of 2D phase *R*-MBA perovskite at low and high temperatures compared to the PL spectrum of the 1D perovskite phase at room temperature. (b) XRD of the corresponding 1D perovskite  $(\text{R-MBA})\text{PbI}_3$  explicitly showing the diffraction corresponding to residual  $\text{PbI}_2$ .

(MBA)PbI<sub>3</sub> PL is dominated by the peak at 535 nm. The high-temperature PL of 2D R-(MBA)<sub>2</sub>PbI<sub>4</sub> can be well reproduced as a superposition of narrow-band low-temperature 2D R-MBA (population of 1D phase not activated) and 1D R-MBA, fully confirming the model presented in Figure 6a. The intense red PL shoulder observed in 1D R-MBA is most likely associated with unreacted PbI<sub>2</sub> in the sample, whose presence is further confirmed by XRD (Figure 8b). When the 1D R-MBA is cooled, the contribution of PbI<sub>2</sub> emission increases (Figure S12), in agreement with the behavior we observed in the 2D phase (Figure 3a).

Interestingly, the enantiomeric composition may affect the radiative properties of the 1D phase, as we systematically observed lower PL values in 1D perovskites based on *rac*-cations (Figure S13). The choice of the cation can also impact the morphology of the 2D material and therefore the relative contribution of the 1D phase, in agreement with Figure 3 observation that (*p*OMeMBA)<sub>2</sub>PbI<sub>4</sub> provides a more symmetric PL spectrum with a weaker shoulder in the 535 nm region.

#### 4. CONCLUSION

In summary, we conclude that the origin of the peak asymmetry and broad emission of 2D chiral MBA-based perovskites at higher temperatures is the presence of a dark excited state, which has a strong nonradiative component and a weak radiative component. This state likely occurs due to the presence of the more thermodynamically stable 1D phase of the material within the 2D perovskite matrix, which forms during synthesis and traps excitons. By substituting a methoxy group on the *para* position of the MBA cation, the phase purity was increased substantially, and this dark state was suppressed. We postulate that the introduction of other electron-donating substitutes may also lead to a similar effect. Our results pinpoint that the broad PL of chiral cation-incorporating halide perovskite compounds is not an intrinsic property and highlight the importance of developing strategies for realizing phase-pure chiral 2D perovskites.

#### ■ ASSOCIATED CONTENT

##### SI Supporting Information

The Supporting Information is available free of charge at <https://pubs.acs.org/doi/10.1021/acs.chemmater.3c03234>.

Description of the experimental techniques; details about DFT calculation; hybrids of resonance of *p*OMeMBA; estimated size of the cations; residual lattice strain; UV–vis and genuine anisotropic factor; PL spectra at 298 and 78 K of the 2D and 1D perovskites; characterization of the 1D perovskite (PDF)

#### ■ AUTHOR INFORMATION

##### Corresponding Authors

**Artem A. Bakulin** – Department of Chemistry and Centre for Processable Electronics, Imperial College London, London W12 0BZ, United Kingdom; [orcid.org/0000-0002-3998-2000](https://orcid.org/0000-0002-3998-2000); Email: [a.bakulin@imperial.ac.uk](mailto:a.bakulin@imperial.ac.uk)

**Yana Vaynzof** – Chair for Emerging Electronic Technologies, Technische Universität Dresden, 01187 Dresden, Germany; Leibniz-Institute for Solid State and Materials Research Dresden, 01069 Dresden, Germany; [orcid.org/0000-0002-0783-0707](https://orcid.org/0000-0002-0783-0707); Email: [y.vaynzof@ifw-dresden.de](mailto:y.vaynzof@ifw-dresden.de)

#### Authors

**Lucas Scalon** – Institute of Chemistry, University of Campinas (UNICAMP), 13083-970 Campinas, São Paulo, Brazil; Chair for Emerging Electronic Technologies, Technische Universität Dresden, 01187 Dresden, Germany; Leibniz-Institute for Solid State and Materials Research Dresden, 01069 Dresden, Germany; [orcid.org/0000-0002-3222-6560](https://orcid.org/0000-0002-3222-6560)

**Arianne New** – Department of Chemistry and Centre for Processable Electronics, Imperial College London, London W12 0BZ, United Kingdom

**Ziyuan Ge** – Department of Chemistry and Centre for Processable Electronics, Imperial College London, London W12 0BZ, United Kingdom; [orcid.org/0000-0001-7820-2073](https://orcid.org/0000-0001-7820-2073)

**Navendu Mondal** – Department of Chemistry and Centre for Processable Electronics, Imperial College London, London W12 0BZ, United Kingdom; [orcid.org/0000-0001-5002-9678](https://orcid.org/0000-0001-5002-9678)

**Raquel Dantas Campos** – Chair for Emerging Electronic Technologies, Technische Universität Dresden, 01187 Dresden, Germany; Leibniz-Institute for Solid State and Materials Research Dresden, 01069 Dresden, Germany

**Claudio Quarti** – Laboratory for Chemistry of Novel Materials, University of Mons–UMONS, Mons 7000, Belgium; [orcid.org/0000-0002-5488-1216](https://orcid.org/0000-0002-5488-1216)

**David Beljonne** – Laboratory for Chemistry of Novel Materials, University of Mons–UMONS, Mons 7000, Belgium; [orcid.org/0000-0002-2989-3557](https://orcid.org/0000-0002-2989-3557)

**Ana Flávia Nogueira** – Institute of Chemistry, University of Campinas (UNICAMP), 13083-970 Campinas, São Paulo, Brazil; [orcid.org/0000-0002-0838-7962](https://orcid.org/0000-0002-0838-7962)

Complete contact information is available at:

<https://pubs.acs.org/doi/10.1021/acs.chemmater.3c03234>

#### Author Contributions

A.B. and Y.V. conceived the idea. L.S. synthesized the materials and performed the structural characterization, circular dichroism, and UV–vis. A.N., Z.G., and N.M. performed and analyzed the temperature-dependent photoluminescence measurements. L.S. and A.N. wrote the original manuscript. R.D.C. performed the SEM measurements. C.Q. and D.B. performed the theoretical calculations. A.B., Y.V., and A.F.N. supervised the project. All the authors revised the final version.

#### Funding

L.S. and A.F.N. gratefully acknowledge support from FAPESP (São Paulo Research Foundation, Grants 2017/11986-5 and 2018/21401-7), Shell, and the strategic importance of the support given by ANP (Brazil's National Oil, Natural Gas, and Biofuels Agency) through the R&D levy regulation. L.S. acknowledges FAPESP (Grants 2020/04406-5 and 2021/12104-1). We also thank the National Council for Scientific and Technological Development (CNPq) and the Center for Innovation on New Energies (CINE). Y.V. thank the Deutsche Forschungsgemeinschaft (DFG) for funding in the framework of the Special Priority Program (SPP 2196) project PERFECT PVs (#424216076.) Computational resources were provided by the Consortium des Équipements de Calcul Intensif (CÉCI) funded by the Belgian National Fund for Scientific Research (F.R.S.-FNRS) under Grant 2.5020.11 and by Tier-1 supercomputer of the Fédération Wallonie–Bruxelles, infrastructure funded by the Walloon Region under the Grant

Agreement 1117545. Part of the work was performed within the frame of the M-ERA.NET project PHANTASTIC (R.8003.22), supported by the FNRS and SMWK. C.Q. is a FNRS Research Associate, and D. B. is FNRS Research Director. Financial support from the DFG through the Würzburg-Dresden Cluster of Excellence on Complexity and Topology in Quantum Matter - ct.qmat (EXC 2147, project-id 390858490) is gratefully acknowledged.

## Notes

The authors declare no competing financial interest.

## ACKNOWLEDGMENTS

The authors thank Yichao Cai for the help with PL spectroscopy of 1D phase samples. L.S. thanks Fernando Abdo Contarim for providing the table of contents graphic.

## REFERENCES

- (1) Ji, R.; Zhang, Z.; Hofstetter, Y. J.; Buschbeck, R.; Hänisch, C.; Paulus, F.; Vaynzof, Y. Perovskite phase heterojunction solar cells. *Nat. Energy* **2022**, *7*, 1170.
- (2) Degani, M.; An, Q.; Albaladejo-Siguan, M.; Hofstetter, Y. J.; Cho, C.; Paulus, F.; Grancini, G.; Vaynzof, Y. 23.7% Efficient inverted perovskite solar cells by dual interfacial modification. *Sci. Adv.* **2021**, *7*, No. eabj7930.
- (3) Scalón, L.; Szostak, R.; Araújo, F. L.; Adriani, K. F.; Silveira, J. F. R. V.; Oliveira, W. X. C.; Da Silva, J. L. F.; Oliveira, C. C.; Nogueira, A. F. Improving the stability and efficiency of perovskite solar cells by a bidentate anilinium salt. *JACS Au* **2022**, *2*, 1306–1312.
- (4) Yassitepe, E.; Yang, Z.; Voznyy, O.; Kim, Y.; Walters, G.; Castañeda, J. A.; Kanjanaboos, P.; Yuan, M.; Gong, X.; Fan, F.; et al. Amine-Free Synthesis of Cesium Lead Halide Perovskite Quantum Dots for Efficient Light-Emitting Diodes. *Adv. Funct. Mater.* **2016**, *26*, 8757–8763.
- (5) Gedda, M.; Gkeka, D.; Nugraha, M. I.; Scaccabarozzi, A. D.; Yengel, E.; Khan, J. I.; Hamilton, I.; Lin, Y.; Deconinck, M.; Vaynzof, Y.; et al. High-efficiency perovskite-organic blend light-emitting diodes featuring self-assembled monolayers as hole-injecting interlayers. *Adv. Energy Mater.* **2023**, *13*, 2201396.
- (6) Chen, W.; Huang, Z.; Yao, H.; Liu, Y.; Zhang, Y.; Li, Z.; Zhou, H.; Xiao, P.; Chen, T.; Sun, H.; et al. Highly bright and stable single-crystal perovskite light-emitting diodes. *Nat. Photonics* **2023**, *17*, 401.
- (7) Marchal, N.; Van Gompel, W.; Gélvez-Rueda, M. C.; Vandewal, K.; Van Hecke, K.; Boyen, H.-G.; Conings, B.; Herckens, R.; Maheshwari, S.; Lutsen, L.; et al. Lead-Halide Perovskites Meet Donor-Acceptor Charge-Transfer Complexes. *Chem. Mater.* **2019**, *31*, 6880–6888.
- (8) Moral, R. F.; Germino, J. C.; Bonato, L. G.; Almeida, D. B.; Therézio, E. M.; Atvars, T. D. Z.; Stranks, S. D.; Nome, R. A.; Nogueira, A. F. Influence of the Vibrational Modes from the Organic Moieties in 2D Lead Halides on Excitonic Recombination and Phase Transition. *Adv. Opt. Mater.* **2020**, *8*, 2001431.
- (9) Long, G.; Jiang, C.; Sabatini, R.; Yang, Z.; Wei, M.; Quan, L. N.; Liang, Q.; Rasmita, A.; Askerka, M.; Walters, G.; et al. Spin control in reduced-dimensional chiral perovskites. *Nat. Photonics* **2018**, *12*, 528–533.
- (10) Pietropaolo, A.; Mattoni, A.; Pica, G.; Fortino, M.; Schifino, G.; Grancini, G. Rationalizing the design and implementation of chiral hybrid perovskites. *Chem.* **2022**, *8*, 1231–1253.
- (11) Liu, Y.; Wang, C.; Guo, Y.; Ma, L.; Zhou, C.; Liu, Y.; Zhu, L.; Li, X.; Zhang, M.; Zhao, G. New lead bromide chiral perovskites with ultra-broadband white-light emission. *J. Mater. Chem. C* **2020**, *8*, 5673–5680.
- (12) Scalón, L.; Vaynzof, Y.; Nogueira, A. F.; Oliveira, C. C. How organic chemistry can affect perovskite photovoltaics. *Cell Rep. Phys. Sci.* **2023**, *4*, 101358.
- (13) Jana, M. K.; Song, R.; Liu, H.; Khanal, D. R.; Janke, S. M.; Zhao, R.; Liu, C.; Vally Vardeny, Z.; Blum, V.; Mitzi, D. B. Organic-to-inorganic structural chirality transfer in a 2D hybrid perovskite and impact on Rashba-Dresselhaus spin-orbit coupling. *Nat. Commun.* **2020**, *11*, 4699.
- (14) Jana, M. K.; Song, R.; Xie, Y.; Zhao, R.; Sercel, P. C.; Blum, V.; Mitzi, D. B. Structural descriptor for enhanced spin-splitting in 2D hybrid perovskites. *Nat. Commun.* **2021**, *12*, 4982.
- (15) Scalón, L.; Brunner, J.; Guaita, M. G. D.; Szostak, R.; Albaladejo-Siguan, M.; Kodalle, T.; Guerrero-León, L. A.; Sutter-Fella, C. M.; Oliveira, C. C.; Vaynzof, Y.; et al. Tuning phase purity in chiral 2D perovskites. *Adv. Opt. Mater.* **2024**, DOI: 10.1002/adom.202300776.
- (16) Di Nuzzo, D.; Cui, L.; Greenfield, J. L.; Zhao, B.; Friend, R. H.; Meskers, S. C. J. Circularly Polarized Photoluminescence from Chiral Perovskite Thin Films at Room Temperature. *ACS Nano* **2020**, *14*, 7610–7616.
- (17) Liu, T.; Shi, W.; Tang, W.; Liu, Z.; Schroeder, B. C.; Fenwick, O.; Fuchter, M. J. High Responsivity Circular Polarized Light Detectors based on Quasi Two-Dimensional Chiral Perovskite Films. *ACS Nano* **2022**, *16*, 2682–2689.
- (18) Li, M.; Wang, Y.; Yang, L.; Chai, Z.; Wang, Y.; Wang, S. Circularly Polarized Radioluminescence from Chiral Perovskite Scintillators for Improved X-ray Imaging. *Angew. Chem.* **2022**, DOI: 10.1002/ange.202208440.
- (19) Son, J.; Ma, S.; Jung, Y.-K.; Tan, J.; Jang, G.; Lee, H.; Lee, C. U.; Lee, J.; Moon, S.; Jeong, W.; et al. Unraveling chirality transfer mechanism by structural isomer-derived hydrogen bonding interaction in 2D chiral perovskite. *Nat. Commun.* **2023**, *14*, 3124.
- (20) Fortino, M.; Mattoni, A.; Pietropaolo, A. Atomistic modeling of metal-ligand chirality transfer and chiroptical properties of lead and tin hybrid perovskites. *J. Mater. Chem. C* **2023**, *11*, 9135.
- (21) Sun, M.-E.; Wang, Y.; Wang, F.; Feng, J.; Wang, L.; Gao, H.; Chen, G.; Gu, J.; Fu, Y.; Bu, K.; et al. Chirality-Dependent Structural Transformation in Chiral 2D Perovskites under High Pressure. *J. Am. Chem. Soc.* **2023**, *145*, 8908–8916.
- (22) Coffey, A. H.; Yang, S. J.; Gómez, M.; Finkenauer, B. P.; Terlier, T.; Zhu, C.; Dou, L. Controlling crystallization of quasi-2D perovskite solar cells: incorporating bulky conjugated ligands. *Adv. Energy Mater.* **2023**, DOI: 10.1002/aenm.202201501.
- (23) Billing, D. G.; Lemmerer, A. Inorganic-organic hybrid materials incorporating primary cyclic ammonium cations: The lead iodide series. *CrystEngComm* **2007**, *9*, 236–244.
- (24) Billing, D. G.; Lemmerer, A. Inorganic-organic hybrid materials incorporating primary cyclic ammonium cations: The lead bromide and chloride series. *CrystEngComm* **2009**, *11*, 1549.
- (25) Han, Y.; Li, Y.; Wang, Y.; Cao, G.; Yue, S.; Zhang, L.; Cui, B.; Chen, Q. From distortion to disconnection: linear alkyl diammonium cations tune structure and photoluminescence of lead bromide perovskites. *Adv. Opt. Mater.* **2020**, DOI: 10.1002/adom.201902051.
- (26) Li, X.; Hoffman, J. M.; Kanatzidis, M. G. The 2D Halide Perovskite Rulebook: How the Spacer Influences Everything from the Structure to Optoelectronic Device Efficiency. *Chem. Rev.* **2021**, *121*, 2230–2291.
- (27) Billing, D. G.; Lemmerer, A. Synthesis and crystal structures of inorganic-organic hybrids incorporating an aromatic amine with a chiral functional group. *CrystEngComm* **2006**, *8*, 686–695.
- (28) Ahn, J.; Lee, E.; Tan, J.; Yang, W.; Kim, B.; Moon, J. A new class of chiral semiconductors: chiral-organic-molecule-incorporating organic-inorganic hybrid perovskites. *Mater. Horiz.* **2017**, *4*, 851–856.
- (29) Ahn, J.; Ma, S.; Kim, J.-Y.; Kyhm, J.; Yang, W.; Lim, J. A.; Kotov, N. A.; Moon, J. Chiral 2D Organic Inorganic Hybrid Perovskite with Circular Dichroism Tunable Over Wide Wavelength Range. *J. Am. Chem. Soc.* **2020**, *142*, 4206–4212.
- (30) Zeng, Y.-L.; Huang, X.-Q.; Huang, C.-R.; Zhang, H.; Wang, F.; Wang, Z.-X. Unprecedented 2D Homochiral Hybrid Lead-Iodide Perovskite Thermochromic Ferroelectrics with Ferroelastic Switching. *Angew. Chem. Int. Ed.* **2021**, *60*, 10730–10735.
- (31) Lee, C. U.; Ma, S.; Ahn, J.; Kyhm, J.; Tan, J.; Lee, H.; Jang, G.; Park, Y. S.; Yun, J.; Lee, J.; et al. Tailoring the Time-Averaged

Structure for Polarization-Sensitive Chiral Perovskites. *J. Am. Chem. Soc.* **2022**, *144*, 16020.

(32) Ma, J.; Fang, C.; Chen, C.; Jin, L.; Wang, J.; Wang, S.; Tang, J.; Li, D. Chiral 2D Perovskites with a High Degree of Circularly Polarized Photoluminescence. *ACS Nano* **2019**, *13*, 3659–3665.

(33) Shpatz Dayan, A.; Wierzbowska, M.; Etgar, L. Ruddlesden-Popper 2D chiral perovskite-based solar cells. *Small Structures* **2022**, *3*, 2200051.

(34) Cortecchia, D.; Neutzner, S.; Srimath Kandada, A. R.; Mosconi, E.; Meggiolaro, D.; De Angelis, F.; Soci, C.; Petrozza, A. Broadband Emission in Two-Dimensional Hybrid Perovskites: The Role of Structural Deformation. *J. Am. Chem. Soc.* **2017**, *139*, 39–42.

(35) Paritmongkol, W.; Powers, E. R.; Dahod, N. S.; Tisdale, W. A. Two origins of broadband emission in multilayered 2D lead iodide perovskites. *J. Phys. Chem. Lett.* **2020**, *11*, 8565–8572.

(36) Smith, M. D.; Jaffe, A.; Dohner, E. R.; Lindenberg, A. M.; Karunadasa, H. I. Structural origins of broadband emission from layered Pb-Br hybrid perovskites. *Chem. Sci.* **2017**, *8*, 4497–4504.

(37) Wheeler, S. E.; Houk, K. N. Substituent effects in the benzene dimer are due to direct interactions of the substituents with the unsubstituted benzene. *J. Am. Chem. Soc.* **2008**, *130*, 10854–10855.

(38) Cockroft, S. L.; Hunter, C. A.; Lawson, K. R.; Perkins, J.; Urch, C. J. Electrostatic control of aromatic stacking interactions. *J. Am. Chem. Soc.* **2005**, *127*, 8594–8595.

(39) Cockroft, S. L.; Perkins, J.; Zonta, C.; Adams, H.; Spey, S. E.; Low, C. M. R.; Vinter, J. G.; Lawson, K. R.; Urch, C. J.; Hunter, C. A. Substituent effects on aromatic stacking interactions. *Org. Biomol. Chem.* **2007**, *5*, 1062–1080.

(40) Vázquez-Cárdenas, R.; Rodríguez-Romero, J.; Echeverría-Arroondo, C.; Sanchez-Díaz, J.; Chirvony, V. S.; Martínez-Pastor, J. P.; Díaz-Leyva, P.; Reyes-Gómez, J.; Zarazua, I.; Mora-Seró, I. Suppressing the Formation of High *n*-Phase and 3D Perovskites in the Fabrication of Ruddlesden-Popper Perovskite Thin Films by Bulky Organic Cation Engineering. *Chem. Mater.* **2022**, *34*, 3076–3088.

(41) Ghosh, D.; Acharya, D.; Pedesseau, L.; Katan, C.; Even, J.; Tretiak, S.; Neukirch, A. J. Charge carrier dynamics in two-dimensional hybrid perovskites: Dion-Jacobson vs Ruddlesden-Popper phases. *J. Mater. Chem. A* **2020**, *8*, 22009–22022.

(42) Cheng, Q.; Wang, B.; Huang, G.; Li, Y.; Li, X.; Chen, J.; Yue, S.; Li, K.; Zhang, H.; Zhang, Y.; et al. Impact of Strain Relaxation on 2D Ruddlesden-Popper Perovskite Solar Cells. *Angew. Chem. Int. Ed* **2022**, *61*, No. e202208264.

(43) Kim, G.; Min, H.; Lee, K. S.; Lee, D. Y.; Yoon, S. M.; Seok, S. I. Impact of strain relaxation on performance of  $\alpha$ -formamidinium lead iodide perovskite solar cells. *Science* **2020**, *370*, 108–112.

(44) Williamson, G. K.; Hall, W. H. X-ray line broadening from filed aluminium and wolfram. *Acta Metall.* **1953**, *1*, 22–31.

(45) Liang, C.; Gu, H.; Xia, Y.; Wang, Z.; Liu, X.; Xia, J.; Zuo, S.; Hu, Y.; Gao, X.; Hui, W.; et al. Two-dimensional Ruddlesden-Popper layered perovskite solar cells based on phase-pure thin films. *Nat. Energy* **2021**, *6*, 38–45.

(46) Liu, Y.; Gao, S.; Chen, C.; Wu, Z.; Gao, P.; Chen, X.; Qin, T. Regulating the Intermolecular Hydrogen Bond to Realize Directional Dimension Reduction of Lead Iodide Perovskite toward Low-Dimensional Photovoltaics. *Langmuir* **2022**, *38*, 7225–7233.

(47) Pedesseau, L.; Saponi, D.; Traore, B.; Robles, R.; Fang, H.-H.; Loi, M. A.; Tsai, H.; Nie, W.; Blancon, J.-C.; Neukirch, A.; et al. Advances and promises of layered halide hybrid perovskite semiconductors. *ACS Nano* **2016**, *10*, 9776–9786.

(48) Quarti, C.; Marchal, N.; Beljonne, D. Tuning the Optoelectronic Properties of Two-Dimensional Hybrid Perovskite Semiconductors with Alkyl Chain Spacers. *J. Phys. Chem. Lett.* **2018**, *9*, 3416–3424.

(49) Dyksik, M.; Duim, H.; Zhu, X.; Yang, Z.; Gen, M.; Kohama, Y.; Adjokatsé, S.; Maude, D. K.; Loi, M. A.; Egger, D. A.; et al. Broad Tunability of Carrier Effective Masses in Two-Dimensional Halide Perovskites. *ACS Energy Lett.* **2020**, *5*, 3609–3616.

(50) Ma, S.; Jung, Y.-K.; Ahn, J.; Kyhm, J.; Tan, J.; Lee, H.; Jang, G.; Lee, C. U.; Walsh, A.; Moon, J. Elucidating the origin of chiroptical activity in chiral 2D perovskites through nano-confined growth. *Nat. Commun.* **2022**, *13*, 3259.

(51) Zhang, Z.; Wang, Z.; Sung, H.H.-Y.; Williams, I. D.; Yu, Z.-G.; Lu, H. Revealing the Intrinsic Chiroptical Activity in Chiral Metal-Halide Semiconductors. *J. Am. Chem. Soc.* **2022**, *144*, 22242.

(52) Yao, Y.; Ugras, T. J.; Meyer, T.; Dykes, M.; Wang, D.; Arbe, A.; Bals, S.; Kahr, B.; Robinson, R. D. Extracting Pure Circular Dichroism from Hierarchically Structured CdS Magic Cluster Films. *ACS Nano* **2022**, *16*, 20457–20469.

(53) Long, G.; Adamo, G.; Tian, J.; Klein, M.; Krishnamoorthy, H. N. S.; Feltri, E.; Wang, H.; Soci, C. Perovskite metasurfaces with large superstructural chirality. *Nat. Commun.* **2022**, *13*, 1551.

(54) Lin, J.-T.; Chen, D.-G.; Yang, L.-S.; Lin, T.-C.; Liu, Y.-H.; Chao, Y.-C.; Chou, P.-T.; Chiu, C.-W. Tuning the Circular Dichroism and Circular Polarized Luminescence Intensities of Chiral 2D Hybrid Organic-Inorganic Perovskites through Halogenation of the Organic Ions. *Angew. Chem. Int. Ed* **2021**, *60*, 21434–21440.

(55) Tan, S.; Zhou, N.; Chen, Y.; Li, L.; Liu, G.; Liu, P.; Zhu, C.; Lu, J.; Sun, W.; Chen, Q. Effect of high dipole moment cation on layered 2D organic-inorganic halide perovskite solar cells. *Adv. Energy Mater.* **2019**, DOI: 10.1002/aenm.201803024.

(56) Smith, M. D.; Pedesseau, L.; Kepenekian, M.; Smith, I. C.; Katan, C.; Even, J.; Karunadasa, H. I. Decreasing the electronic confinement in layered perovskites through intercalation. *Chem. Sci.* **2017**, *8*, 1960–1968.

(57) Baibarac, M.; Preda, N.; Mihut, L.; Baltog, I.; Lefrant, S.; Mevellec, J. Y. On the optical properties of micro- and nanometric size PbI<sub>2</sub> particles. *J. Phys.: Condens. Matter* **2004**, *16*, 2345–2356.

(58) Booker, E. P.; Price, M. B.; Budden, P. J.; Abolins, H.; del Valle-Inclan Redondo, Y.; Eyre, L.; Nasrallah, I.; Phillips, R. T.; Friend, R. H.; Deschler, F.; et al. Vertical cavity biexciton lasing in 2D dodecylammonium lead iodide perovskites. *Adv. Opt. Mater.* **2018**, *6*, 1800616.

(59) Kaiser, M.; Li, Y.; Schwenzler, J.; Jakoby, M.; Allegro, I.; Gerhard, M.; Koch, M.; Ducinkas, A.; Richards, B. S.; Graetzel, M.; et al. How free exciton-exciton annihilation lets bound exciton emission dominate the photoluminescence of 2D-perovskites under high-fluence pulsed excitation at cryogenic temperatures. *J. Appl. Phys.* **2021**, *129*, 123101.

(60) Thirumal, K.; Chong, W. K.; Xie, W.; Ganguly, R.; Muduli, S. K.; Sherburne, M.; Asta, M.; Mhaisalkar, S.; Sum, T. C.; Soo, H. S.; et al. Morphology-Independent Stable White-Light Emission from Self-Assembled Two-Dimensional Perovskites Driven by Strong Exciton-Phonon Coupling to the Organic Framework. *Chem. Mater.* **2017**, *29*, 3947–3953.

(61) Dohner, E. R.; Jaffe, A.; Bradshaw, L. R.; Karunadasa, H. I. Intrinsic white-light emission from layered hybrid perovskites. *J. Am. Chem. Soc.* **2014**, *136*, 13154–13157.

(62) Wang, Y.; He, C.; Tan, Q.; Tang, Z.; Huang, L.; Liu, L.; Yin, J.; Jiang, Y.; Wang, X.; Pan, A. Exciton-phonon coupling in two-dimensional layered (BA)<sub>2</sub>PbI<sub>4</sub> perovskite microplates. *RSC Adv.* **2023**, *13*, 5893–5899.

(63) Feldstein, D.; Perea-Causín, R.; Wang, S.; Dyksik, M.; Watanabe, K.; Taniguchi, T.; Plochocka, P.; Malic, E. Microscopic Picture of Electron-Phonon Interaction in Two-Dimensional Halide Perovskites. *J. Phys. Chem. Lett.* **2020**, *11*, 9975–9982.

(64) Gan, Z.; Wen, X.; Zhou, C.; Chen, W.; Zheng, F.; Yang, S.; Davis, J. A.; Tapping, P. C.; Kee, T. W.; Zhang, H.; et al. Transient energy reservoir in 2D perovskites. *Adv. Opt. Mater.* **2019**, *7*, 1900971.

(65) Folpini, G.; Cortecchia, D.; Petrozza, A.; Srimath Kandada, A. R. The role of a dark exciton reservoir in the luminescence efficiency of two-dimensional tin iodide perovskites. *J. Mater. Chem. C* **2020**, *8*, 10889–10896.

(66) Hu, T.; Smith, M. D.; Dohner, E. R.; Sher, M.-J.; Wu, X.; Trinh, M. T.; Fisher, A.; Corbett, J.; Zhu, X. Y.; Karunadasa, H. I.; et al. Mechanism for Broadband White-Light Emission from Two-Dimen-

sional (110) Hybrid Perovskites. *J. Phys. Chem. Lett.* **2016**, *7*, 2258–2263.

(67) Zhang, L.; Wu, L.; Wang, K.; Zou, B. Pressure-Induced Broadband Emission of 2D Organic-Inorganic Hybrid Perovskite ( $C_6H_5C_2H_4NH_3$ )<sub>2</sub>PbBr<sub>4</sub>. *Adv. Sci. (Weinh)* **2019**, *6*, 1801628.

(68) Pareja-Rivera, C.; Morán-Muñoz, J. A.; Gómora-Figueroa, A. P.; Jancik, V.; Vargas, B.; Rodríguez-Hernández, J.; Solís-Ibarra, D. Optimizing broadband emission in 2D halide perovskites. *Chem. Mater.* **2022**, *34*, 9344–9349.

(69) Kahmann, S.; Meggiolaro, D.; Gregori, L.; Tekelenburg, E. K.; Pitaro, M.; Stranks, S. D.; De Angelis, F.; Loi, M. A. The Origin of Broad Emission in  $\langle 100 \rangle$  Two-Dimensional Perovskites: Extrinsic vs Intrinsic Processes. *ACS Energy Lett.* **2022**, *7*, 4232–4241.

(70) Billings, D. G. Bis(1-phenylethylammonium) tetraiodoplumbate(II). *Acta Crystallogr. E Struct. Rep. Online* **2002**, *58*, m669–m671.

(71) Tanaka, K.; Takahashi, T.; Kondo, T.; Umeda, K.; Ema, K.; Umebayashi, T.; Asai, K.; Uchida, K.; Miura, N. Electronic and Excitonic Structures of Inorganic-Organic Perovskite-Type Quantum-Well Crystal ( $C_4H_9NH_3$ )<sub>2</sub>PbBr<sub>4</sub>. *Jpn. J. Appl. Phys.* **2005**, *44*, 5923–5932.

(72) Dyksik, M.; Duim, H.; Maude, D. K.; Baranowski, M.; Loi, M. A.; Plochocka, P. Brightening of dark excitons in 2D perovskites. *Sci. Adv.* **2021**, *7*, No. eabk0904.

(73) Quarti, C.; Giorgi, G.; Katan, C.; Even, J.; Palummo, M. Exciton Ground State Fine Structure and Excited States Landscape in Layered Halide Perovskites from Combined BSE Simulations and Symmetry Analysis. *Adv. Opt. Mater.* **2023**, 2202801.

(74) Tamarat, P.; Bodnarchuk, M. I.; Trebbia, J.-B.; Erni, R.; Kovalenko, M. V.; Even, J.; Lounis, B. The ground exciton state of formamidinium lead bromide perovskite nanocrystals is a singlet dark state. *Nat. Mater.* **2019**, *18*, 717–724.

(75) Kilinkissa, O. E. Y.; Govender, K. K.; Báthori, N. B. Melting point-solubility-structure correlations in chiral and racemic model cocrystals. *CrystEngComm* **2020**, *22*, 2766–2771.

(76) Quan, L. N.; Yuan, M.; Comin, R.; Voznyy, O.; Beauregard, E. M.; Hoogland, S.; Buin, A.; Kirmani, A. R.; Zhao, K.; Amassian, A.; et al. Ligand-Stabilized Reduced-Dimensionality Perovskites. *J. Am. Chem. Soc.* **2016**, *138*, 2649–2655.

(77) Bakthavatsalam, R.; Haris, M. P. U.; Shaikh, S. R.; Lohar, A.; Mohanty, A.; Moghe, D.; Sharma, S.; Biswas, C.; Raavi, S. S. K.; Gonnade, R. G.; et al. Ligand structure directed dimensionality reduction (2D  $\rightarrow$  1D) in lead bromide perovskite. *J. Phys. Chem. C* **2020**, *124*, 1888–1897.